12th International Conference on Fracture Mechanics of Concrete and Concrete Structures
FraMCoS-12
B.L.A. Pichler, Ch. Hellmich, P. Preinstorfer (Eds)

https://doi.org/10.21012/FC12.1201
MS02-2:4

STRUCTURAL COMPRESSIVE FATIGUE SIMULATED VIA LATTICE DISCRETE AND MICROPLANE MODELS

Mario Aguilar[1], **Miroslav Vořechovský**[2], **Abedulgader Baktheer**[1], **Rostislav Chudoba**[1]

[1] Institute of Structural Concrete, RWTH Aachen University,
Mies-van-der-Rohe-Str. 1 52074 Aachen, Germany, maguilar@imb.rwth-aachen.de

[2] Institute of Structural Mechanics, Brno University of Technology,
Veveří 95, 602 00 Brno, Czech Republic

Key words: Cohesive Fracture, Fiber Reinforced Concrete, Composites, Durability

Abstract. Accurate prediction of structural fatigue life under compression is crucial for infrastructure safety, yet the fatigue behavior of concrete remains insufficiently understood. This study proposes a dissipation hypothesis linking fatigue-induced degradation to cumulative inter-aggregate shear strain, leading to a pressure-sensitive interface model embedded in both discrete and microplane formulations. To validate this hypothesis, extensive experimental and numerical studies were conducted, including cylinder compression test of varying sizes, concrete mixes, and loading frequencies, alongside prestressed four-point bending tests representing structural compressive fatigue. Results indicate that direct transfer of fatigue data from cylinder tests to structural components is inadequate. Therefore, a detailed discrete mesoscale model of the prestressed four-point bending test was developed to further analyze and interpret structural fatigue damage. The mesoscale model, which uses a lattice-discrete material idealization, is qualitatively compared with numerical studies performed using FE and the microplane model MS1. The studies include a comparison of the shape of hysteretic loops, stress redistribution along the cross-section, and the shape of energy dissipation profiles.

1 INTRODUCTION

Compressive fatigue research in high-performance reinforced concrete (RC) structures is critical due to the high material utilization in modern designs, particularly in prestressed, slender structures such as wind turbine towers [2, 3, 4]. Significant progress has been made in understanding the fatigue properties of concrete, with research addressing various influencing factors. These include loading frequency and temperature [5, 6, 7, 8], moisture [9, 10, 11], loading sequences [12, 13], and multiaxial behaviour [14, 15, 16]. Although S-N curves derived from cylindrical specimens [17] serve as the basis for fatigue assessment in design codes, transferring these findings to structural components remains a significant challenge.

To experimentally investigate the structural compressive fatigue behavior of concrete, a test setup originally presented in [1] was used. The setup involved an externally prestressed bending test on an inverted T-beam subjected to four-point bending. The beam had a span of 1.4m, a height of 25 cm, and chord and web widths of 25 cm and 7 cm respectively. The beam, presented in Fig. 1 was designed to maximize compressive stress at the top surface, initiating compressive fatigue failure in the compression zone, which then propagates downwards through the cross-section. Two vertical single loads were applied to induce the bending

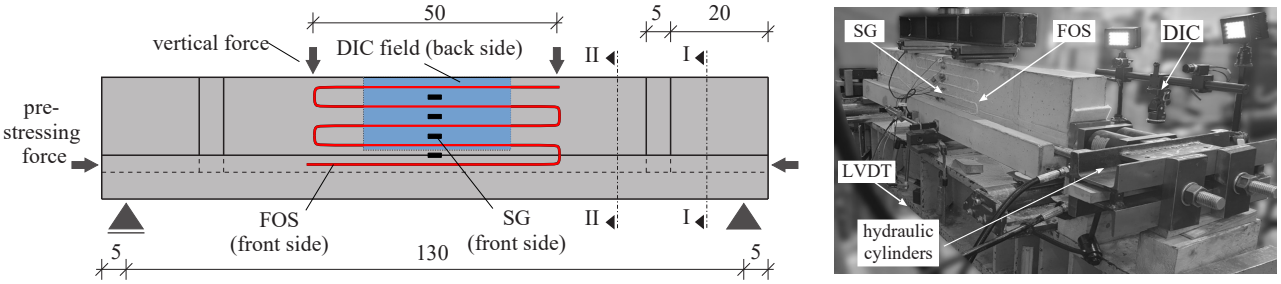

Figure 1: Considered test setups and the used measurement techniques for the externally prestressed bending test presented at [1]

moment, as shown in Fig. 1. In addition, the beam was externally prestressed with an eccentric normal force to prevent tensile cracking at the bottom.

Advanced monitoring techniques such as digital image correlation were used to analyze the propagation of fatigue damage in the compression zone [1]. For a deeper interpretation of the experimental results, numerical analyses were performed using a unified framework that links material and structural fatigue behavior. This framework incorporates a thermodynamically based formulation of an interface material model that describes the fatigue behavior of cementitious materials at the mesoscale level. The framework includes: (a) the microplane model MS1, developed within the microplane framework and combined with finite element (FE) analysis [18], and (b) MARS, a lattice discrete particle model framework [19].

The aims of this paper are: (I) to validate the constitutive hypothesis by predicting structural compressive fatigue in a lattice discrete model using material model parameters calibrated from cylindrical specimens [20], and (II) to analyze and compare the propagation of compressive fatigue and stress redistribution using both the microplane model MS1 in combination with FE and the lattice discrete model, employing consistent constitutive hypothesis.

2 THERMODYNAMIC FORMULATION

To capture the fatigue behavior of concrete, a constitutive framework grounded in thermodynamic principles has been developed, as elaborated in detail in [21]. This framework enables the derivation of an interface model that can be applied either within a generic microplane model or at the inter-aggregate contact level in a lattice discrete particle model. The approach is predicated on the assumption that fatigue damage evolution in concrete is predominantly influenced by the cumulative inelastic shear strain occurring at inter-aggregate contacts [22, 21]. This hypothesis has been proven valuable in describing the fatigue behavior of concrete under compression, tension and multi-axial loading [18, 23, 24, 25, 26, 16].

2.1 Free energy potential, state variables and thermodynamic forces

The interface-relative displacement between two connected points is characterized by a normal (out-of-plane) component, denoted as $u_\mathrm{N} \equiv u_z$, and an (in-plane) sliding vector $\boldsymbol{u}_\mathrm{T} = \{u_x, u_y\}^\mathsf{T}$. The kinematic variables governing the irreversible state of the interface are expressed as

$$\mathcal{E} := \left[u_\mathrm{N}^\mathrm{p},\ \omega_\mathrm{N}, \boldsymbol{u}_\mathrm{T}^\mathrm{p},\ \omega_\mathrm{T},\ z,\ \boldsymbol{\alpha}\right]. \qquad (1)$$

To distinctly represent the dissipative mechanisms in the normal and tangential directions, the free energy is formulated as a sum of contributions from opening (N) and sliding (T)

$$\rho\psi(\mathcal{E}) := \rho\psi_\mathrm{N}(\mathcal{E}) + \rho\psi_\mathrm{T}(\mathcal{E}). \qquad (2)$$

The free energy associated with normal interface behavior (opening/closing) is defined as a function of total displacement u_N, plastic displacement u_N^p, and damage ω_N as

$$\rho\psi_{\mathrm{N}} := \frac{1}{2}\,(1 - H(\sigma_{\mathrm{N}})\,\omega_{\mathrm{N}})\,E_{\mathrm{N}}(u_{\mathrm{N}} - u_{\mathrm{N}}^{\mathrm{p}})^2, \quad (3)$$

where E_{N} represents the stiffness, and the Heaviside function $H(.)$ ensures damage activation only under tensile stress σ_{N}. The free energy associated with the interface sliding is defined as a function of total sliding vector $\boldsymbol{u}_{\mathrm{T}}$, plastic sliding vector $\boldsymbol{u}_{\mathrm{T}}^{\mathrm{p}}$, tangential damage ω_{T}, and the displacement variables corresponding to isotropic and kinematic hardening, z and $\boldsymbol{\alpha} = [\alpha_x, \alpha_y]$, respectively, as

$$\rho\psi_{\mathrm{T}} := \frac{1}{2}(1-\omega_{\mathrm{T}})E_{\mathrm{T}}\left[(\boldsymbol{u}_{\mathrm{T}} - \boldsymbol{u}_{\mathrm{T}}^{\mathrm{p}})^{\mathsf{T}} \cdot (\boldsymbol{u}_{\mathrm{T}} - \boldsymbol{u}_{\mathrm{T}}^{\mathrm{p}})\right] + \frac{1}{2}Kz^2 + \frac{1}{2}\gamma(\boldsymbol{\alpha}^{\mathsf{T}} \cdot \boldsymbol{\alpha}), \quad (4)$$

where E_{T} denotes the tangential stiffness, K the isotropic and γ the kinematic hardening moduli. The thermodynamic forces are obtained by differentiating the free energy with respect to the kinematic state variables

$$\mathcal{S} = \boldsymbol{\Upsilon}\,\frac{\partial \rho\psi(\mathcal{E})}{\partial \mathcal{E}}. \quad (5)$$

The sign vector operator $\boldsymbol{\Upsilon}$ is introduced to render positive thermodynamic force for positive state variable. To distinguish the thermodynamic forces based on the in correspondence with the definition of the state vector in Eq. (1), let us introduce the generalized vector of thermodynamic forces as

$$\mathcal{S} := \left[\sigma_{\mathrm{N}}^{\mathrm{p}},\, Y_{\mathrm{N}},\, \boldsymbol{\sigma}_{\mathrm{T}}^{\mathrm{p}},\, Y_{\mathrm{T}},\, Z,\, \boldsymbol{X}\right]. \quad (6)$$

The individual components of this vector can be obtained using Eq. (5) and their expressions can be found at [21].

3 MICROPLANE MODEL

In contrast to traditional constitutive models that define a direct relationship between the strain and stress *tensors*, microplane models establish constitutive relationships between strain and stress *vectors* on individual projected planes, thereby capturing the anisotropic characteristics of concrete more effectively.

Kinematic constraint: The strain tensor is projected onto each microplane to derive strain vectors, comprising normal and tangential components, through the application of the kinematic constraint.

$$\varepsilon_{\mathrm{N}} = \boldsymbol{N} : \boldsymbol{\varepsilon}, \qquad \boldsymbol{\varepsilon}_{\mathrm{T}} = \mathrm{T} : \boldsymbol{\varepsilon}, \quad (7)$$

Here, the scalar ε_{N} represents the normal microplane strain, while $\boldsymbol{\varepsilon}_{\mathrm{T}}$ denotes the tangential microplane strain vector. The second-order normal tensor $\boldsymbol{N}$ and the third-order tangential tensor $\boldsymbol{T}$ are defined as:

$$\boldsymbol{N} = \boldsymbol{n} \otimes \boldsymbol{n}, \qquad \mathrm{T} = \boldsymbol{n} \cdot \mathbb{I}_{sym} - \boldsymbol{n} \otimes \boldsymbol{n} \otimes \boldsymbol{n}, \quad (8)$$

In this context, $\boldsymbol{n}$ denotes the microplane normal vector, and $\mathbb{I}$ represents the fourth-order identity tensor.

Constitutive behavior: The constitutive response of the proposed microplane model is governed by the thermodynamically derived constitutive laws detailed in Sec. 2, which describe the macroscopic behavior. These laws are formulated on generic microplanes and incorporate dissipative mechanisms for both the normal and tangential directions.

Homogenization: The macroscopic stress tensor can be obtained as follows

$$\boldsymbol{\sigma} = \boldsymbol{\beta} : \boldsymbol{C}^{\mathrm{e}} : \boldsymbol{\beta}^{\mathrm{T}} : (\boldsymbol{\varepsilon} - \boldsymbol{\varepsilon}^{\mathrm{p}}). \quad (9)$$

Here, $\boldsymbol{\beta}$ represents the fourth-order damage inverse (or integrity) tensor, $\boldsymbol{C}^{\mathrm{e}}$ is the fourth-order elasticity tensor, and $\boldsymbol{\varepsilon}^{\mathrm{p}}$ denotes the macroscopic plastic strain tensor. As demonstrated in [27], the macroscopic plastic strain tensor can be determined by integrating the plastic strains from individual microplanes as

$$\boldsymbol{\varepsilon}_{ij}^{p} = \frac{3}{2\pi}\int_{\Omega} \varepsilon_{N}^{p,\mathrm{mic}} n_i n_j \,\mathrm{d}\Omega + \frac{3}{2\pi}\int_{\Omega} \frac{\varepsilon_{Tr}^{\pi,\mathrm{mic}}}{2}(n_i\delta_{rj} + n_j\delta_{ri})\,\mathrm{d}\Omega. \quad (10)$$

The fourth-order damage inverse (or integrity) tensor $\boldsymbol{\beta}$ is derived by integrating the normal

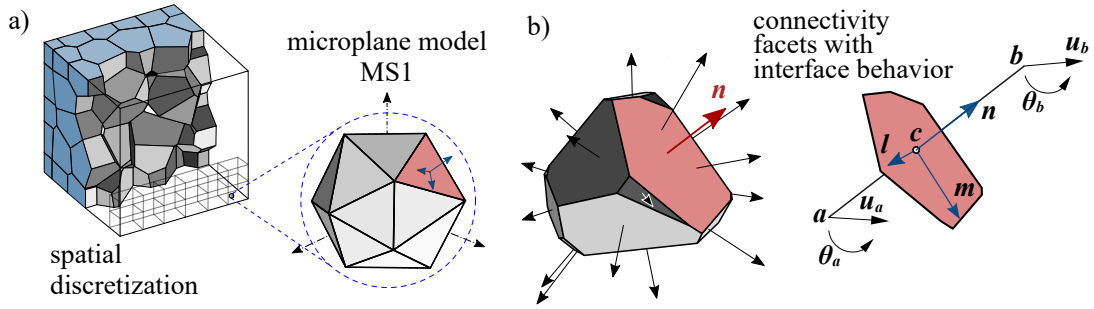

Figure 2: a) Cell with connections to neighboring particle centers, b) Contact facet between particles associated with nodes $\boldsymbol{a}$ and $\boldsymbol{b}$.

and tangential damage parameters of the microplanes

$$\boldsymbol{\beta}_{ijkl} = \frac{3}{2\pi}\int_\Omega \beta_N\, n_i\, n_j\, n_k\, n_l\, \mathrm{d}\Omega + \frac{3}{2\pi}\int_\Omega \frac{\beta_T}{4} \left(n_i\, n_k \delta_{jl} + n_i\, n_l \delta_{jk} + n_j\, n_k \delta_{il} + n_j\, n_l \delta_{ik} - 4 n_i\, n_j\, n_k\, n_l\right) \mathrm{d}\Omega. \quad (11)$$

Here, $\beta_N^{\mathrm{mic}} = \sqrt{1-\omega_N^{\mathrm{mic}}}$ represents the integrity parameter in the normal direction, while $\beta_T^{\mathrm{mic}} = \sqrt{1-\omega_T^{\mathrm{mic}}}$ corresponds to the integrity parameter in the tangential direction.

Following the homogenization of the microplane state variables, the macroscopic stress-strain relationship is established. This allows the constitutive equations to be implemented as a material subroutine within a finite element (FE) package, enabling further computations within a spatial discretization framework, as in Fig. 2a.

4 LATTICE DISCRETE MODEL

The lattice discrete particle model (LDPM), integrated with the aforementioned constitutive model, is utilized for explicit simulations of concrete's mesostructure [28]. This approach represents the material as a network of particles possessing both translational and rotational degrees of freedom. Larger aggregates are modeled as rigid particles surrounded by a cement matrix, while smaller aggregates are excluded, with their effects being incorporated into the constitutive laws governing the interactions between the larger particles. The model's kinematics are governed by the rigid-body motion of the particles, leading to displacement jumps at their interfaces.

Spatial domain discretization: The internal structure of the material is defined using Delaunay triangulation, which links the centers of the rigid particles representing the aggregates to form the lattice system. A tessellation of the domain then creates a network of polyhedral cells, each containing an aggregate surrounded by the cement matrix. Interactions between aggregates take place through the facets of the polyhedral cells shared by adjacent particles.

Kinematics: The displacement vector $\boldsymbol{u}_p = \begin{bmatrix} u_1^p & u_2^p & u_3^p \end{bmatrix}$ of any point $\boldsymbol{p}$ within a rigid body can be expressed in terms of the displacements $\boldsymbol{u}_a$ of the governing particle node $\boldsymbol{a}$ and the rotations $\boldsymbol{\theta}_a$ of rigid body a, as outlined in [29]

$$\boldsymbol{u}_p = \boldsymbol{u}_a + \boldsymbol{\theta}_a \times (\boldsymbol{p} - \boldsymbol{a}) = \boldsymbol{A}_a^p \boldsymbol{q} \quad (12)$$

where the vector $\boldsymbol{q}$ is collecting the displacements and rotations

$$\boldsymbol{q}^{\mathsf{T}} = \begin{bmatrix} u_1^a & u_2^a & u_3^a & \theta_1^a & \theta_2^a & \theta_3^a \end{bmatrix}, \quad (13)$$

and

$$\boldsymbol{A}_a^p = \begin{bmatrix} 1 & 0 & 0 & 0 & x_3^p - x_3^a & x_2^a - x_2^p \\ 0 & 1 & 0 & x_3^a - x_3^p & 0 & x_1^p - x_1^a \\ 0 & 0 & 1 & x_2^p - x_2^a & x_1^a - x_1^p & 0 \end{bmatrix}. \quad (14)$$

The subscripts 1, 2, and 3 correspond to the three coordinate directions. In this description

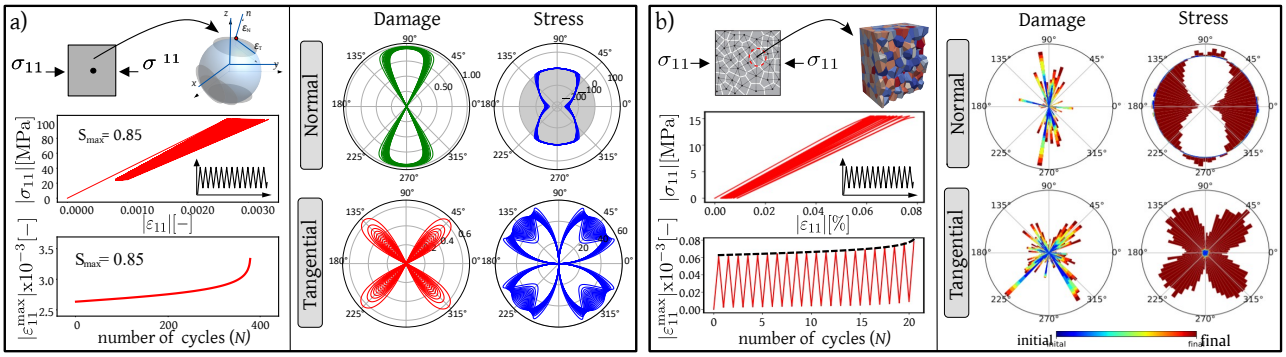

Figure 3: Elementary studies of: a) the 2D microplane model and b) the lattice discrete model under cyclic/fatigue compressive loading, illustrating stress redistribution at the microplane level and within a material zone: a) left: the macroscopic response of a single material point; b) of a material zone; b) right: the evolution and distribution of strains, damage, plastic strains, and stresses at each microplane, and b) right for a material zone.

of rigid body motion, small deformations and rotations are assumed. Consider two rigid bodies, a and b, sharing a common contact facet, as shown in Fig. 2b. Assuming arbitrary displacements and rotations for both a and b, the displacement of point c at the contact facet can be obtained by substituting the coordinates of c with those of a and b into Eq.(14). The displacement difference on either side of the contact facet leads to the following expression for the displacement jump between rigid bodies a and b at the centroid of the contact facet, $\boldsymbol{c}$

$$\Delta \boldsymbol{u}_{ab} = \boldsymbol{A}_b^c (\boldsymbol{u}_b \boldsymbol{\theta}_b)^T - \boldsymbol{A}_a^c (\boldsymbol{u}_a \boldsymbol{\theta}_a)^T \qquad (15)$$

Stress-displacement relation: The interaction between particles is governed by constitutive relations applied at their contact facets. The mesoscale elastic behavior is defined by two parameters: the elastic interface stiffness in the normal direction, E_N, and in the tangential direction, E_T, both with unit of [Pa/m]. The relationship between stress, σ, and displacements, $\boldsymbol{u}$, in the elastic regime for each facet is expressed as

$$\begin{Bmatrix} \sigma_N \\ \sigma_M \\ \sigma_L \end{Bmatrix} = \begin{bmatrix} E_\mathrm{N} & & \\ & E_\mathrm{T} & \\ & & E_\mathrm{T} \end{bmatrix} \begin{Bmatrix} u_N \\ u_M \\ u_L \end{Bmatrix}. \qquad (16)$$

In nonlinear regime, the contact constitutive behavior comes from the relations described in Sec. 2.

Balance equation: The solution for the unknown displacements is obtained by enforcing the principle of virtual work. This involves balancing the work done by forces (forces $\boldsymbol{f}_a$, $\boldsymbol{f}_b$, and moments $\boldsymbol{m}_a$, $\boldsymbol{m}_b$) acting on the virtual nodal displacements ($\delta\boldsymbol{u}_a$, $\delta\boldsymbol{u}_b$, and $\delta\boldsymbol{\theta}a$, $\delta\boldsymbol{\theta}b$) with the work done by forces ($\boldsymbol{s}$ from Eq. 16, scaled by the contact area A) acting on the virtual displacement jumps at the facet ($\delta\boldsymbol{\Delta u}ab = L, \delta\boldsymbol{e}ab$):

$$\begin{pmatrix} \boldsymbol{f}_a & \boldsymbol{m}_a & \boldsymbol{f}_b & \boldsymbol{m}_b \end{pmatrix} \begin{pmatrix} \delta\boldsymbol{u}_a & \delta\boldsymbol{\theta}_a & \delta\boldsymbol{u}_b & \delta\boldsymbol{\theta}_b \end{pmatrix}^T = A\,\boldsymbol{\sigma}^T \delta\boldsymbol{\Delta u}_{ab} \qquad (17)$$

5 NUMERICAL STUDIES

5.1 MATERIAL FATIGUE

First, to verify the proposed constitutive model under a well-established stress state, Fig. 3 presents material zone-level simulations using the microplane and mesoscale discrete models. These simulations examine their response to subcritical compressive cyclic loading and their ability to capture stress redistribution within an idealized material structure. In Fig. 3a, the microplane model simulates compressive fatigue at loading levels $S_\mathrm{max} = 0.85$ and $S_\mathrm{min} = 0.20$. Polar plots illustrate the evolution of damage and stress at each microplane over load cycles, highlighting the model's ability to realistically replicate fatigue-induced anisotropic dam-

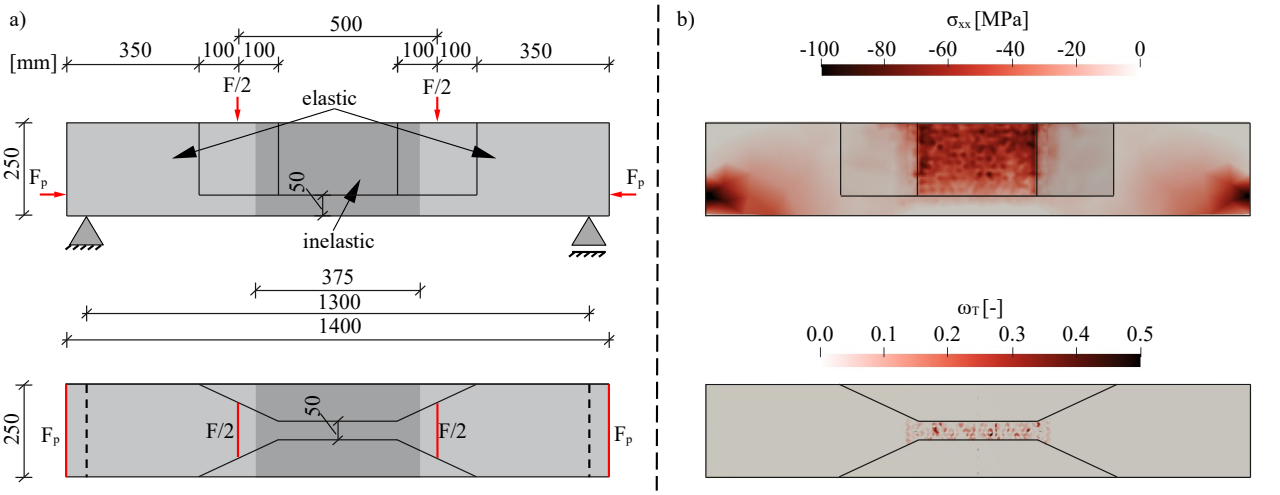

Figure 4: Boudary conditions of the mesoscale discrete model with visualized stress and damage fields after application of 600 kN precompression and 360 kN of vertical loading.

age and stress redistribution. Similarly, Fig. 3b illustrates a study using the mesoscale discrete model, where the state variables associated with the normal direction of each facet are shown in polar plots, with the first and last cycles shown in blue and red, respectively. Both models show similar patterns of normal and tangential damage distribution along with their corresponding stress profiles. These results indicate that the microplane model, despite being a semi-multiscale approach, effectively homogenizes stress at the inter-aggregate level, allowing for efficient fatigue simulations. However, its inability to explicitly represent the spatial mesostructure of concrete limits its ability to capture key structural phenomena such as damage localization, crack propagation, and aggregate interlocking, which are inherently addressed by the mesoscale discrete model.

5.2 STRUCTURAL FATIGUE

The ability to capture the fatigue degradation of a structure with spatially non-uniform stress state is exemplified using a four point bending test. A simulation of the prestressed beam using a mesoscale discrete idealization is compared with the results of a similar beam modeled using the microplane fatigue model MS1 and finite elements (FE). Both beams are identical in length, width, and height. The geometry and boundary conditions of the discrete model are shown in Fig. 4a. The distribution of macroscopic horizontal stresses and tangential damage after the application of a prestressing of 600 kN and a bending force of 360 kN is shown in Fig. 4b. The weakened cross section in both models differs by stiffed flange, as shown schematically in Fig. 6. Detailed geometry and numerical results for the microplane model MS1 are presented in [24].

The simulation of the pre-stressed bending test setup using macroscopic and mesoscale models highlights the limitations, advantages, inconveniences, and scope of applicability of each model.

5.3 QUALITATIVE COMPARISON

To reduce the computational cost of the fatigue simulation in the finite element (FE) model, only a quarter of the beam was modeled using symmetry axes. The region in the middle of the beam span, where damage localization is expected in the compression zone, was modeled with nonlinear material behavior using the MS1 fatigue model. The remaining parts of the beam were modeled as elastic material. The beam was discretized using 3D tetrahedral elements with a size of 0.03 m, resulting in a total of 4598 elements. A prestressing force of 618 kN was applied. The upper and lower fatigue load levels for the applied bending actions

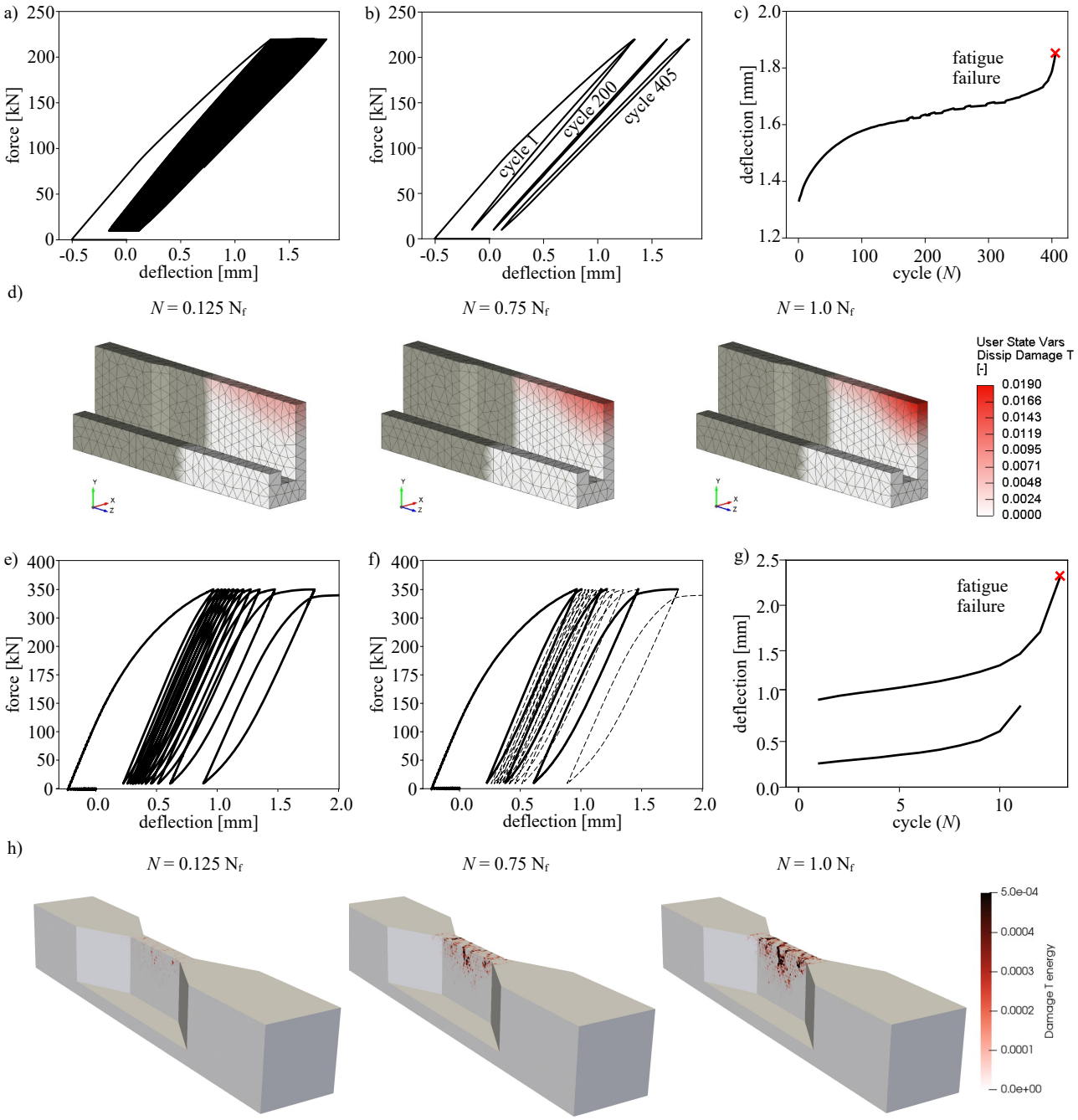

Figure 5: Simulation of an externally prestressed bending test: a) load-deflection response under fatigue loading using MS1 and FE; b) load-deflection response of three selected loading cycles using MS1 and FE; c) corresponding fatigue creep curve using MS1 and FE; d) contour plots of tangential damage dissipated energy using MS1 and FE; e) load-deflection response under fatigue loading using mesoscale discrete idealization; f) load-deflection response of three selected loading cycles using mesoscale discrete idealization; g) corresponding fatigue creep curve using mesoscale discrete idealization; h) contour plots of tangential damage dissipated energy using mesoscale discrete idealization.

were $F_{\max} = 219.6$ kN and $F_{\min} = 9.8$ kN, respectively. More details can be found in [24].

Additionally, to reduce the computational cost of the mesoscale discrete model, outer regions where no significant inelastic phenomena occur were modeled using elastic material and coarser aggregate size. These regions are shown in

Fig. 4. The minimum and maximum aggregate sizes in the elastic region were set to 30 mm and 60 mm, respectively, while in the inelastic region, they were set to 8 mm and 16 mm, respectively. A prestressing force of 600 kN was applied, with cyclic bending loading ranging from 360 kN to 10 kN. The material parameters for the inelastic region were obtained from [20].

Since the primary objective of this study is to evaluate the plausibility of both models in simulating compressive fatigue propagation and stress redistribution, an accelerated fatigue simulation was performed. Higher force levels than those used in the experiments [1] were applied to induce fatigue failure while maintaining reasonable computational cost for a cycle-by-cycle simulation. Despite these adjustments, the simulations allow the evaluation of key fatigue characteristics and a comparative analysis of the microplane and mesoscale discrete models.

The simulated load-deflection response under fatigue loading using the microplane model is shown in Figure 5a, which represents the complete loading history. The beam experienced fatigue failure after 405 cycles. To provide insight into the shape of the hysteretic loops, specific load cycles were plotted in Figure 5b, including the first load cycle, cycle 200, and the last load cycle (cycle 405). A realistic evolution in the shape of the hysteretic loops can be observed, as the loops in stages I and III are wider than those in stage II, effectively reproducing the known fatigue phenomenology of concrete.

The corresponding fatigue creep curve, which illustrates the deformation increment during the fatigue life at the upper load level, is shown in Figure 5c. The curve exhibits the three stages of fatigue tests, with rapid deformation growth in the early and late stages and nearly linear, moderate deformation growth in the intermediate stage [30, 31], which is a consequence of the previously commented change of shape of the hysteretic loops. In particular, the model accurately captures the first branch of the fatigue creep curve, which is characterized by a decreasing rate of inelastic deformation as a structural effect. This phenomenon was not reproducible in the single material point simulations presented in [18].

To visualize the localization leading to fatigue failure, contour plots of tangential damage dissipation are presented for the simulated one-quarter of the beam at three stages during fatigue loading, as shown in Fig. 5d. The contour plots clearly show the development and propagation of compressive fatigue, particularly in the upper-middle region of the beam. This observation agrees remarkably well with the experimental results of beam B2 in [1]. Comparison of the contour plots with the experimental data indicates that the model accurately reproduces the compressive fatigue behavior observed in concrete members.

The numerical results from the mesoscale discrete model are presented below. Figure 5e depicts the force-deflection curve, showing that the beam experienced fatigue failure after 12 cycles. The loading amplitude was deliberately set high to induce rapid fatigue failure due to the significant computational cost of the simulation. Despite this constraint, several key features of the model's behavior can be observed. The shape of the hysteretic loops, as illustrated in Fig. 5e, appears highly realistic. Additionally, Fig. 5f highlights three specific cycles from the loading history for closer examination.

In this mesoscale discrete simulation, the variation in hysteretic loop widths, typically indicative of the three phases of concrete fatigue, is not observable. Similarly, the creep-fatigue curve in Fig. 5g does not exhibit the three distinct fatigue phases. This limitation is due to the short fatigue life modeled, effectively skipping the transition from I to II and transitioning directly from phase II to III. A simulation with a lower loading amplitude and therefore extended fatigue life is necessary to show that the model captures all three phases. This capability is plausible, as the microplane model has successfully reproduced these stages, and the material models governing individual mi-

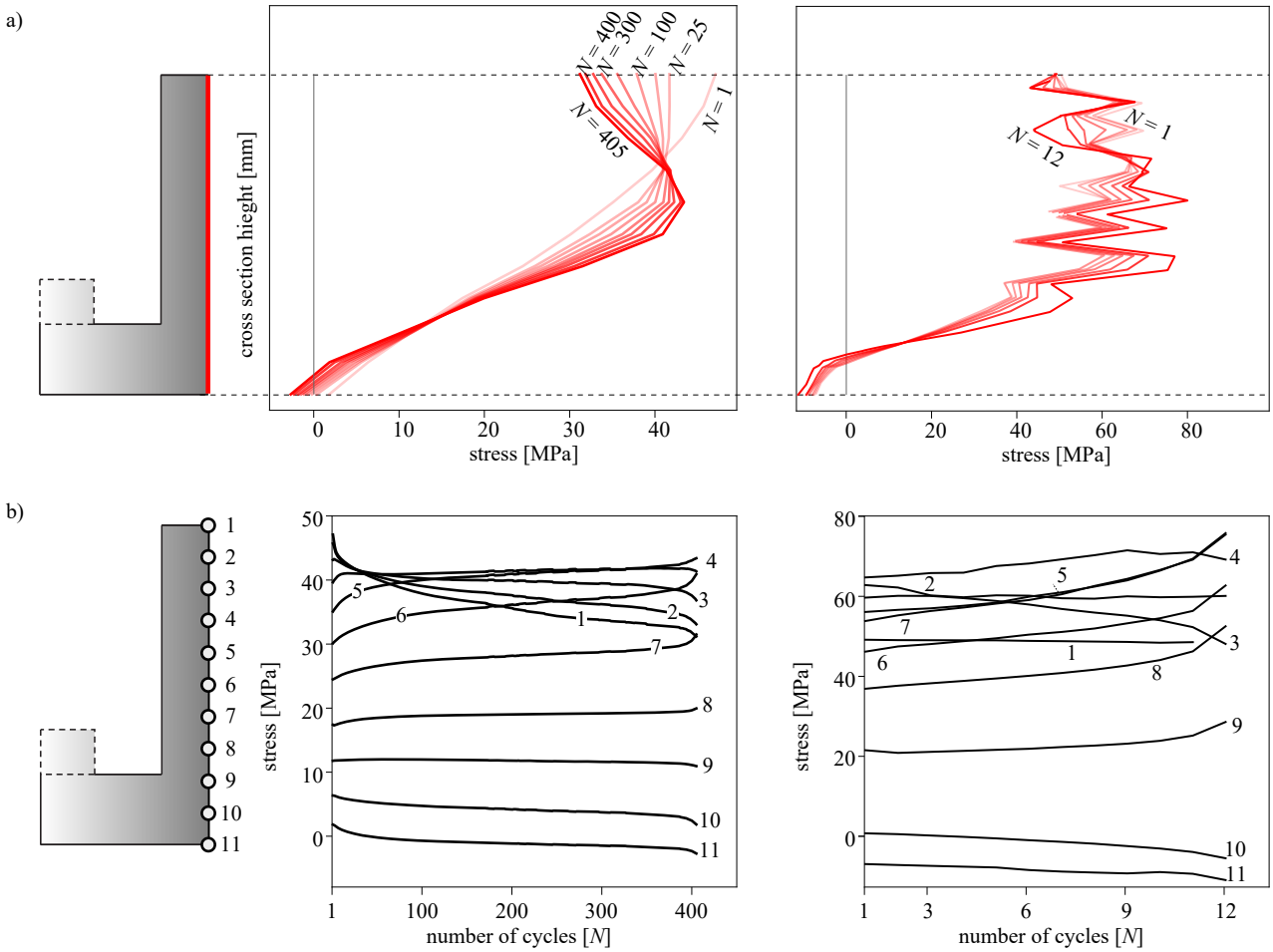

Figure 6: Stress development in the simulated prestressed bending test, on the left results obtained using MS1 and FE and on the right results obtained using the lattice discrete model: a) stress profiles over the mid-span cross-section for selected loading cycles; b) stress evolution during fatigue life obtained for several points over the mid-span cross-section

croplanes and facet-level interfaces are based on the same dissipation hypothesis. Furthermore, as a mesoscale model, the discrete approach provides a more detailed and realistic depiction of material behavior compared to macroscopic models.

To examine the localization leading to fatigue failure, Fig. 5h presents contour plots of tangential damage dissipation at three stages during fatigue loading. These plots clearly demonstrate the localization of fatigue damage in the top-center region of the weakened section. The observed localization patterns are more realistic than the smeared patterns produced by the microplane model and are qualitatively consistent with results obtained via digital image correlation (DIC). These findings inspire significant confidence in the proposed model, particularly as it represents a direct prediction of the structural response using material parameters calibrated to fit the compressive strength and S-N curve of a cylinder.

5.4 FATIGUE DAMAGE PROPAGATION

The stress profiles obtained numerically using finite elements and the MS1 model are shown on the left side of Fig. 6a. The evolution of these profiles during fatigue loading highlights a significant phenomenon: stress redistribution at the structural level. Comparing the stress profiles from the first and last load cycles reveals this effect clearly. Specifically, stresses at the top fiber decrease due to fatigue-induced deteri-

oration, while stresses above the middle portion of the cross-section increase.

On the right side of Fig. 6a, the stress profiles obtained from the mesoscale discrete simulation are presented. During the first cycle, stresses in the upper section of the beam are higher compared to those in cycle twelve, while the central region shows an opposite trend. This behavior aligns with results from the microplane model MS1. However, two key distinctions are observed. First, the stress profile is notably irregular, reflecting the inherently discrete nature of the mesoscale model. Second, stresses at the top fiber of the beam remain constant during cyclic loading. This outcome is attributable to the high loading amplitude, which caused substantial damage in the top region of the beam during the first cycle. This is evident in the contour plot of tangential damage shown in Fig. 4, where significant damage values were reached after the peak of the initial cycle. As a result, stress was rapidly redistributed to the lower regions.

Despite these differences, the results from both models exhibit a comparable general trend of stress redistribution during fatigue loading. This is further emphasized in Fig. 6b, which depicts the evolution of stresses at various points across the cross-sectional height.

6 CONCLUSIONS

The MS1 microplane model and the discrete fatigue model are valuable methods for investigating the structural fatigue behavior of concrete members. These models effectively capture the progression of compressive fatigue and accurately simulate the stress redistribution phenomenon observed in an externally prestressed bending test. The energy dissipation profiles derived from the thermodynamic formulation of the models are in close agreement for both models, as are the stress redistribution profiles. Furthermore, the hysteretic loops under subcritical cyclic loading realistically illustrate damage accumulation during unloading, in agreement with experimental observations.

ACKNOWLEDGEMENT

The work was supported within the framework of the joint project, supporting the German partner by the German Research Foundation (DFG), project number 471796896, and the Czech partner (M. Vořechovský) by the Czech Science Foundation, project number GF22-06684K. We gratefully acknowledge ES3inc for providing MARS, which significantly contributed to the completion of this research.

REFERENCES

[1] H. Becks, A. Baktheer, S. Marx, M. Classen, J. Hegger, R. Chudoba, Monitoring concept for the propagation of compressive fatigue in externally prestressed concrete beams using digital image correlation and fiber optic sensors, Fatigue & Fracture of Engineering Materials & Structures 46 (2) (2023) 514–526. doi:10.1111/ffe.13881.

[2] S. Marx, J. Grünberg, M. Hansen, S. Schneider, DAfStb Heft 618, Sachstandbericht-Grenzzustände der Ermüdung von dynamisch hoch beanspruchten Tragwerken aus Beton, Beuth Verlag GmbH, 2017.

[3] B. Schmidt, S. Schneider, S. Marx, Concrete fatigue-safety and development potential of current design concepts, Bautechnik 96 (4) (2019) 329–337.

[4] A. Baktheer, C. Goralski, J. Hegger, R. Chudoba, Stress configuration-based classification of current research on fatigue of reinforced and prestressed concrete, Structural Concrete (2024). doi:10.1002/suco.202300667.

[5] S. Schneider, D. Vöcker, S. Marx, Zum Einfluss der Belastungsfrequenz und der Spannungsgeschwindigkeit auf die Ermüdungsfestigkeit von Beton, Beton- und Stahlbetonbau 107 (12) (2012) 836–845. doi:10.1002/best.201200054.

[6] K. Elsmeier, J. Hümme, N. Oneschkow, L. Lohaus, Prüftechnische Einflüsse

auf das Ermüdungsverhalten hochfester feinkörniger Vergussbetone, Beton- und Stahlbetonbau 111 (4) (2016) 233–240. doi:10.1002/best.201500065.

[7] C. Otto, K. Elsmeier, L. Lohaus, Temperature effects on the fatigue resistance of high-strength-concrete and high-strength-grout, High Tech Concrete: Where Technology and Engineering Meet, Springer International Publishing, Cham, 2018, pp. 1401–1409.

[8] M. Deutscher, N. L. Tran, S. Scheerer, Experimental investigations on temperature generation and release of ultra-high performance concrete during fatigue tests, Applied Sciences 10 (17) (2020). doi:10.3390/app10175845.

[9] C. Tomann, N. Oneschkow, Influence of moisture content in the microstructure on the fatigue deterioration of high-strength concrete, Structural Concrete 20 (4) (2019) 1204–1211. doi:10.1002/suco.201900023.

[10] M. Markert, J. Katzmann, V. Birtel, H. Garrecht, H. Steeb, Investigation of the influence of moisture content on fatigue behaviour of hpc by using dma and xrct, Materials 15 (1) (2022). doi:10.3390/ma15010091.

[11] M. Abubakar Ali, C. Tomann, F. Aldakheel, M. Mahlbacher, N. Noii, N. Oneschkow, K.-H. Drake, L. Lohaus, P. Wriggers, M. Haist, Influence of moisture content and wet environment on the fatigue behaviour of high-strength concrete, Materials 15 (3) (2022). doi:10.3390/ma15031025.

[12] G. Petkovic, R. Lenschow, H. Stemland, S. Rosseland, Fatigue of high-strength concrete, ACI Special Publication 121 (1990) 505–526. doi:10.14359/3740.

[13] A. Baktheer, R. Chudoba, Experimental and theoretical evidence for the load sequence effect in the compressive fatigue behavior of concrete, Materials and Structures 54 (2) (2021) 82. doi:10.1617/s11527-021-01667-0.

[14] K. V. Subramaniam, J. S. Popovics, S. P. Shah, Fatigue fracture of concrete subjected to biaxial stresses in the tensile c-t region, J Eng Mech. 128 (6) (2002) 668–676.

[15] D. Zhao, H. Gao, H. Liu, P. Jia, J. Yang, Fatigue properties of plain concrete under triaxial tension-compression-compression cyclic loading, Shock Vib. 2017 (2017) 1–10.

[16] M. Aguilar, A. Baktheer, R. Chudoba, Multi-axial fatigue of high-strength concrete: Model-enabled interpretation of punch-through shear test response, Engineering Fracture Mechanics 311 (2024) 110532. doi:https://doi.org/10.1016/j.engfracmech.2024.110532. URL https://www.sciencedirect.com/science/article/pii/S0013794424006957

[17] N. Oneschkow, Fatigue behaviour of high-strength concrete with respect to strain and stiffness, International Journal of Fatigue 87 (2016) 38 – 49. doi:10.1016/j.ijfatigue.2016.01.008.

[18] A. Baktheer, M. Aguilar, R. Chudoba, Microplane fatigue model MS1 for plain concrete under compression with damage evolution driven by cumulative inelastic shear strain, International Journal of Plasticity 143 (2021). doi:10.1016/j.ijplas.2021.102950.

[19] A. Cibelli, R. Wan-Wendner, L. Wan-Wendner, J. Vorel, D. Pelessone, MARS–a multiphysics framework for the analysis of cast and printed concrete, DBMC 2023 (2023).

[20] M. Aguilar, A. Baktheer, R. Wan-Wendner, J. Vorel, M. Vorechovskỳ, R. Chudoba, Simulation of tri-axial stress redistribution effect in concrete under fa-

tigue loading: Lattice discrete model vs. microplane model.

[21] R. Chudoba, M. Vořechovský, M. Aguilar, A. Baktheer, Coupled sliding–decohesion–compression model for a consistent description of monotonic and fatigue behavior of material interfaces, Computer Methods in Applied Mechanics and Engineering 398 (2022) 115259. doi:10.1016/j.cma.2022.115259.

[22] A. Baktheer, R. Chudoba, Pressure-sensitive bond fatigue model with damage evolution driven by cumulative slip: Thermodynamic formulation and applications to steel- and frp-concrete bond, International Journal of Fatigue 113 (2018) 277 – 289. doi:10.1016/j.ijfatigue.2018.04.020.

[23] A. Baktheer, M. Aguilar, J. Hegger, R. Chudoba, Microplane damage plastic model for plain concrete subjected to compressive fatigue loading, 10th International Conference on Fracture Mechanics of Concrete and Concrete Structures, FraMCoS-X, 2019. doi:10.21012/FC10.233196.

[24] A. Baktheer, S. Esfandiari, M. Aguilar, H. Becks, M. Classen, R. Chudoba, Fatigue-induced stress redistribution in prestressed concrete beams modeled using the constitutive hypothesis of inter-aggregate degradation, Fatigue & Fracture of Engineering Materials & Structures 47 (10) (2024) 3673–3692. doi:10.1111/ffe.14388.

[25] M. Aguilar, A. Baktheer, R. Chudoba, On the energy dissipation in confined concrete subjected to shear cyclic loading, Proceedings in Applied Mathematics and Mechanics 22 (1) (2023) e202200301. doi:10.1002/pamm.202200301.

[26] M. Aguilar, A. Baktheer, H. Becks, M. Classen, R. Chudoba, Fatigue-induced concrete fracture under combined compression and shear studied using standard cylinder and refined punch-through shear test setup, 11th International Conference on Fracture Mechanics of Concrete and Concrete Structures (2023). doi:10.21012/FC11.092350.

[27] I. Carol, Z. P. Bažant, Damage and plasticity in microplane theory, International Journal of Solids and Structures 34 (29) (1997) 3807–3835. doi:10.1016/S0020-7683(96)00238-7.

[28] J. E. Bolander, J. Eliáš, G. Cusatis, K. Nagai, Discrete mechanical models of concrete fracture, Engineering Fracture Mechanics 257 (2021) 108030. doi:10.1016/j.engfracmech.2021.108030.

[29] G. Cusatis, D. Pelessone, A. Mencarelli, Lattice discrete particle model (ldpm) for failure behavior of concrete. i: Theory, Cement and Concrete Composites 33 (9) (2011) 881 – 890. doi:10.1016/j.cemconcomp.2011.02.011.

[30] J.-K. Kim, Y.-Y. Kim, Experimental study of the fatigue behavior of high strength concrete, Cement and Concrete Research 26 (10) (1996) 1513 – 1523. doi:10.1016/0008-8846(96)00151-2.

[31] M. Classen, J. Gallwoszus, Concrete fatigue in composite dowels, Structural Concrete 17 (1) (2016) 63–73. doi:10.1002/suco.201400120.